Partial rupture of a locked patch of the Sumatra megathrust during the 2007 earthquake sequence

A. Ozgun Konca[1], Jean-Philippe Avouac[1], Anthony Sladen[1], Aron J. Meltzner[1], Kerry Sieh[1], Peng Fang[2], Zhenhong Li[3], John Galetzka[1], Jeff Genrich[1], Mohamed Chlieh[4], Danny H. Natawidjaja[1], Yehuda Bock[2], Eric J. Fielding[5], Chen Ji[6], and Don V. Helmberger[1]

Supplementary Information

A. GPS data and processing

The data processing was carried out using GAMIT/GLOBK version 10.31 (http://chandler.mit.edu/~simon/gtgk/GAMIT_Ref_10.3.pdf). A total of 9 days of observations from 2007 Sept 8 to Sept 16 were used. Data, sampled at a 120 s interval, were processed in daily sessions except on the days of the M_w 8.4 and 7.9 earthquakes. On these days we computed sub-daily sessions from the set of 120s samples determined before and after each quake. For each session, a regional network is formed consisting of the regional sites and selected nearby global sites. The global sites are: COCO, DGAR, GUAM, IISC, NTUS, PERT and TIDB. International GNSS Service (IGS) final orbits (http://igscb.jpl.nasa.gov) and International Earth Rotation Service (IERS Bulletin-A) final earth orientation parameters (http://maia.usno.navy.mil) were used with tight constraints. Standard corrections were applied including solid earth tides, pole tide, and ocean tides. Tropospheric delay parameters were estimated at one hour intervals.

After completing individual daily/sub-daily sessions using GAMIT, the loosely constrained solutions were sorted into four groups: one before the 1st quake, one after the 1st quake and before the 2nd, one after the 2nd and before the 3rd, and one after the 3rd. They were input to the GLOBK software and combined with SOPAC final global solutions (http://garner.ucsd.edu/pub/solutions/global) in order to tie the solutions to the ITRF2005 global reference frame http://itrf.ensg.ign.fr/ITRF_solutions/2005/ITRF2005.php. The formal uncertainties for individual sites for those 4 grouped time segments are given in Tables S1-S3. The data can be visualized and downloaded from the Caltech Tectonics Observatory web site (http://www.tectonics.caltech.edu/sumatra/data.html).

Co-seismic offsets are measured as the difference of the average position determined from the position time series between the two earthquakes, compared to linear least squares adjustment of the position time series before the 1st and after the 2nd earthquake. This process allows measuring the sudden offset at the time of each earthquake.

B. Measurements of uplift from emerged coral heads

Coral microatolls of the genus *Porites* are sensitive natural recorders of lowest tide levels [1-4], and as such they are ideal natural instruments for measuring emergence or submergence relative to a tidal datum. Massive *Porites* coral heads grow radially upward

and outward until they reach an elevation that exposes their highest corallites to the atmosphere during lowest tides. This subaerial exposure kills the uppermost corallites in the colony, thus restricting future upward growth. The highest level to which a coral can grow is termed the highest level of survival (HLS). If a coral microatoll is then uplifted or subsides, its morphology preserves information about relative water level prior to the land level change [2, 4].

When coseismic uplift occurs, those portions of the microatoll colony raised above lowest tides die, but if lower parts of the coral head are still below lowest tides, its uppermost living tissues demarcate a new, post-earthquake HLS [2]. Coral microatolls have been shown to track annual low tide (ALT, the lowest low tide of any given year) with an accuracy of a few centimeters, [3] and the difference between pre-earthquake and post-earthquake HLS can be taken as the amount of uplift. In cases of subsidence or where post-earthquake HLS cannot be found, the elevation change can be determined using the pre-earthquake HLS and post-earthquake calculated ALT[4, 5].

The corals revealed significant uplift of Mega Island, South Pagai Island, and the northern tip of Sipora Island. The maximum uplift measured from corals was 1.3 m, on Mega Island, about 70 km northwest of the epicenter. Uplift decreases northward to about 1 meter on southern South Pagai, to 10 cm on North Pagai Island. The uplift on northern Sipora Island is on the order of 20-30 cm (inset in Figure 2a, Table S4).

C. InSAR data and processing

We processed four independent L-band interferograms from ALOS PALSAR images using the ROI_PAC software[6] and the satellite orbits provided by JAXA with the PALSAR data (Table S5). The topographic phase contribution was removed using a 3 arc.s (~90 m) digital elevation model from the Shuttle Radar Topography Mission (SRTM)[7]. The interferograms were next unwrapped to obtain line-of-sight (LOS) displacements, i.e., along a direction that is pointing approximately N78^{o}E with an incidence angle of 38° from vertical. Typical PALSAR raw data in the Fine Beam Single (FBS) polarization mode has a row width of ~10500 pixels, exactly twice that of Fine Beam Double (FBD) polarization images [8]. In order to make a mixed-mode interferogram (FBS2FBD) for track 445, the FBD was up-sampled by FFT [9].

Even in heavily vegetated areas, coherence is generally good and deformation is well resolved, highlighting the main advantage of L-band (wavelength of 23.53 cm) over C-band (wavelength of 5.66 cm): i.e. less temporal decorrelation due to its capability to penetrate more deeply in vegetation. The track 448 pair, in which coherence degrades rapidly in areas of rugged terrain in the south part of South Pagai Island, is explained by the large perpendicular baseline (506 m, Table 1). Because most interferograms do not extend far enough from the area with significant ground displacements, possible orbit knowledge errors were not corrected a priori. Instead, we allow for a ramp correction (first order polynomial) in the LOS displacement field that is solved for during the joint inversion.

The interferograms were unwrapped using the SNAPHU algorithm [10]. The unwrapped interferograms were resampled by averaging phase with variable block sizes using a fault slip resolution-based algorithm [11] and are shown in Figure 2b. The resampling process reduced the number of InSAR data samples from millions to about 400 samples per interferogram. The LOS vector was approximated as constant over the PALSAR tracks.

InSAR data show that there is strong gradient in displacement under the Pagai Islands (track 448), while displacement under Siberut is insignificant (track 450). The tracks along the Sumatra coast show a deep slip patch near Bengkulu (track 445 and 446). Overall, the InSAR data is in very good agreement with cGPS and coral data.

D. Effect of post-seismic slip on the geodetic data and Cumulative Model

We have used three different sets of geodetic data—continuous GPS (cGPS), InSAR and coral uplift measurements—to model the cumulative slip from the 2007 Sumatra sequence (Figure 2a). Inspection of the time series shows that the co-seismic displacements measured from cGPS data are probably not biased by post-seismic deformation. By contrast, the coral and InSAR measurements cover a time span which is longer than the coseismic earthquake duration, over which some postseismic deformation occurred as the GPS time series reveal. Post-seismic horizontal displacements in the month following the earthquakes are as great as 50% of the coseismic signal, but for the stations with the largest offsets (BSAT, PRKB) they remain less than 35% of the co-seismic offset measured from the daily solution. Preliminary modeling show that postseismic deformation is due mainly to rapidly decaying afterslip updip of the rupture area (as was observed following the M_w 8.6 Nias-Simeulue earthquake[12]) and released a geodetic moment of about 10^{21}N.m over the 125 days following the mainshock, representing about 15% of the co-seismic moment.

Pre-earthquake images of the InSAR data were acquired in the month prior to the earthquake except one track (track 445) where the pre-earthquake image was obtained 9 months before the earthquakes. Acquisition of the post-earthquake images occurred between 4 days and 43 days after the earthquake. The GPS time series shows that the preseismic signal in these data is insignificant. The postseismic signal, however, could represent as much as 35% of the signal measured on Siberut (track 450) and Pagai Islands but is probably a smaller fraction of the signal measured from the other tracks, since they were all acquired less than 20 days after the mainshock (Table S5). The coral measurements were made 2.5 to 4 weeks after the earthquake (Table S4). Therefore these measurements might also be influenced by post-seismic motion of up to 35 % of the measurement values.

One way to test effect of the post-seismic slip in our cumulative model from all geodetic data (cGPS, InSAR and corals) is to compare it to the models that do not include coral and InSAR data. Figure S2a shows a cumulative slip model obtained using only the cGPS displacements measured from just before the M_w 8.4 to just after the M_w 7.9. The model using cGPS data only, suggests a relatively patchy slip distribution with a geodetic

moment of 7.3 × 10^{21}N.m. The best-fitting model calculated from all three geodetic datasets (Figure 2a) has a total moment of 7.5 × 10^{21} N.m (equivalent to M_w 8.5) which is only marginally larger than the one derived from the cGPS measurements alone.

The cumulative source model from all geodetic data is also very similar to the cumulative slip obtained by adding up the coseismic slip models of M_w 8.4 and M_w 7.9 earthquakes along with an M_w 7 aftershock located at the northwest tip of Sipora (Figure S2b; see Table S6 for model parameters). The model obtained by the addition of individual events is more confined along dip and has a lower moment (6.3 × 10^{21}N.m). This implies that including coral and InSAR data does introduce some post-seismic contamination. Nevertheless, the models obtained from cGPS only and from the addition of coseismic slips are very similar to the geodetic model utilizing all available data. Considering the advantage of greater resolution afforded by the coral and InSAR measurements, we regard the source model using all geodetic data to be a better-constrained representation of the cumulative slip distribution.

E. ***Fault geometry***

There are no good geophysical constraints on the megathrust geometry in the Mentawai area. The global Centroid-Moment Tensor solutions show a dip angle of about 9° for the M_w 8.4 and 19° for the M_w 7.9 event (http://www.globalcmt.org/) that might suggest lateral variations, down-dip variations, or variations in both, of the dip angle.

However, for simplicity we have approximated the megathrust geometry as a planar fault dipping 15° to the northeast. This dip angle is consistent with the geometry of the megathrust beneath the forearc as can be inferred from various geophysical data including relocated seismicity[13], seismic profiles[14] and gravity modeling. [15] We found that we can reconcile all the data to first order from this simple assumption.

The modeled mainshock fault plane consists of 16 km by 16 km sub-faults, whereas the fault plane is more finely gridded (12 km by 10 km) for the M_w 7.9 event. In order to test the sensitivity of our results to the assumed megathrust geometry we also computed a model assuming an increase of the dip angle from 10º beneath the Mentawai Islands to 20º beneath the forearc basin and Sumatra mainland coastal area (Figure S3). Figure S3 shows for example the slip distribution obtained from the modeling of coral, cGPS and InSAR data. The slip distribution is only slightly different from that obtained with the reference single planar fault model. The total released moment, 7.79× 10^{21} N.m, is only 9% higher. The number and the location of the main asperities, as well the values of the peak slip are nearly identical to the reference model as well.

F. Resolution Test

We have carried out checkerboard tests to evaluate the spatial resolution in our inversions (Figure S4). This approach only applies to the geodetic models which are in fact the key data constraining the geographic distribution of the slip. The resolution of the joint

inversions must be similar or even better due to the additional constraints brought by the seismic waveform modeling, but this cannot be tested easily from checkerboard tests.

We constructed two checkerboard models, one with 48 × 48 km patches and the other with 80 × 80 km patches. We computed the corresponding theoretical displacements at the cGPS stations and at the location where coral data were collected, and the synthetic InSAR data a well (Figure 2a). The results of the checkerboard tests show that the slip patches of 80 km by 80 km are well resolved over most of the study area (Figure S4a). The 48 km by 48 km slip patches (Figure S4b) are well resolved in the Pagai and Sipora islands area and beneath the mainland, where most of the slip actually occurred in the 2007 events. The slip patches to the south of the Pagai Islands are not well resolved at this scale.

G. Source models of the M_w 8.4 and M_w 7.9 earthquakes

We derived separate source models of the mainshock (M_w 8.4) and principal aftershock (M_w 7.9) using teleseismic waveforms, GPS measurements, and subsets of the coral and InSAR data. To guide selection of the coral and InSAR data relevant to the modeling of each event we first carried out an inversion of just the teleseismic data first and then included the GPS data. The slip distribution derived from the inversion of the teleseismic waveforms only are shown in Figure S5 (details on these models are available at http://www.tectonics.caltech.edu/slip_history/index.html). The fit to the teleseismic and InSAR data, of the source models derived from joint inversion for the M_w 8.4 and 7.9 earthquakes, respectively, are shown in Figures S6 and S7.

The source model of the M_w 8.4 earthquake derived from the inversion of the teleseismic waveforms show a rather diffuse slip distribution with slip spread along the isochrons. This is typical for teleseismic models when the source is not very impulsive, as is the case here, and is usually more severe for subduction earthquakes which tend to be wider along dip than crustal earthquakes. Although these models fit the teleseismic records very well they are not consistent with the geodetic data. When the GPS data are included in the inversion, the fit to seismological data is not degraded; this shows that the two dataset are consistent but that the GPS data put tighter constraints on the spatial distribution of slip. The geodetic data show that slip was confined to a narrower zone along dip with a larger maximum slip than the teleseismic inversion suggests (Figure S8). The teleseismic model of the M_w 7.9 earthquake (Figure S5b) is closer to the model derived from the joint inversion (Figure 2c). This is because the sharp initial pulse in the teleseismic waves (Figure S7) requires rupture of a rather compact first asperity near the hypocenter. The teleseismic records also require a second asperity which is estimated to lie near Sipora Island from the inversion.

Separating the effects of the two events on the measured co-seismic displacements in the region of the Pagai Islands, where their rupture areas abut or overlap, is most challenging. In this region, the coral and InSAR measurements (PALSAR track 448 from the Pagai Islands and track 446 from the Sumatra mainland coast, Figure S1) contain components from both events. Farther south and east, the displacements measured along PALSAR track 445 and coral measurements on Mega Island are clearly attributable to the

mainshock alone. Since track 445 includes only 4 days of post-seismic slip, we chose to take it into account to constrain the source of the mainshock. We inverted these subsets of the coral and InSAR data together with the GPS measurements and the teleseismic records of that earthquake. We initially used the US Geological Survey (USGS) hypocenter and origin time (http://earthquake.usgs.gov/) to model the earthquakes. The M_w 8.4 earthquake model fits the teleseismic waveforms and geodetic data very well using the hypocenter reported by the USGS (lon: 101.382°, lat:-4.517°).

Fitting the geodetic and teleseismic data of the M_w 7.9 earthquake was more challenging when epicenter reported by USGS was used. The cGPS measurements on the Sumatra mainland show subsidence and modest horizontal displacements, while the measurements on South Pagai Island reveal significant uplift and more trenchward horizontal displacement (Figure 2c). Therefore, cGPS data require a slip patch just east of South Pagai Island (Figure 2c). In addition, sharp initial pulses in teleseismic waveforms require a slip patch centered at the hypocenter. We were unable to fit the geodetic and teleseismic data using the epicenter reported by USGS (lon: 100.964°, lat: -2.525°), which is just offshore the Sumatra mainland. Obtaining satisfactory fits to both datasets requires that the hypocenter lies at the center of the slip patch that is constrained from geodesy. Thus, we moved the M_w 7.9 epicenter east of South Pagai (lon: 100.5°, lat: -2.75°), about 55 km southwest of the USGS epicenter, and were thus able to reconcile all the data reasonably well. So, the addition of the geodetic and InSAR data essentially lead to some slight shift of the geographic location of the two asperities derived from the inversion of the teleseismic records alone.

H. Significance of the surface deformation north of Bengkulu

Both the GPS and InSAR data indicate a deep slip patch beneath an area north of Bengkulu. The evidence from cGPS data comes from LAIS station, which subsided only 10 cm but moved 70 cm trenchwards during the M_w 8.4 mainshock. Assuming that all the slip has occurred on the megathrust, the only plausible explanation of this low ratio of vertical to horizontal displacement is to invoke some slip patch east of this station (Figure S9). Varying the dip angle does not improve the fits to the GPS data from LAIS station unless slip on downdip side of this station is allowed. The fault geometry with a depth dependent dip angle reveals the same result (Figure S3). The two InSAR tracks along the Sumatra coast (tracks 445 and 446 of Figure S1) provide a much denser spatial coverage and help constrain the shape and location of this slip patch (Figure 2b, Figure S3). Since the deformation is observed in these two independent tracks, the possibility of an atmospheric artifact can be excluded.

This deep slip patch had to occur during the mainshock rupture, because the sampling rate at LAIS is 120 s and the displacements shown in Figure 2b occurred within the 120-s period that includes the mainshock. The corresponding moment of this patch is around 6.3×10^{20} N.m (~M_w 7.8) assuming a shear modulus of 67.5 GPa. Despite the significant moment release, whether this patch radiated some seismic energy is unclear. Removal of the patch from the mainshock model yields only marginally different seismic waveforms and source time function (Figure S10).

In our model, the megathrust dips uniformly 15 degrees from the trench, so that this slip patch lies at a depth of about 90 km. It is more plausible, however, that the megathrust lies at a depth of about 120 km at the location of the patch given that the dip angle must increase down-dip. Another possibility would be that this deformation did not take place on the megathrust but at shallower depths. The available data do not resolve the ambiguity.

I. ***Goodness of fit criterion and normalization of uncertainties***

In order to obtain the best-fitting models, we use an optimization method based on simulated annealing algorithm, where bounded parameter spaces of slip amplitude, rake angle and the rupture velocity are searched to obtain models that fit both teleseismic and geodetic data[16].

The seismic modeling requires fitting the wavelet transform of seismograms. The seismic displacements are calculated by

$$u(t)=\sum_{j=1}^{n}\sum_{k=1}^{m} D_{jk}\cdot Y_{jk}\left(\vec{x},t-d_{jk}/V_{jk}\right)\cdot \dot{S}_{jk}(t)\ , \quad (1)$$

where $u(t)$ is the displacement at the station, j and k are indices of summation along strike and dip, respectively, Y_{jk} are the sub-fault Green's functions, D_{jk} the dislocations, V_{jk} are the rupture velocities between the hypocenter and sub-faults and d_{jk} are the distance of the sub-fault from the hypocenter. The rise time for each element is given by $S_{jk}(t)$. Both the V_{jk}'s and $S_{jk}(t)$'s control the timing of the contribution from each sub-fault. We approximate the latter as a modified cosine function defined by one parameter, as first proposed by Cotton and Campillo[17]. These seismograms are then transformed to wavelet domain to use the time and frequency variations in the signal simultaneously.

The misfit between the observation and synthetic waveforms is then quantified by the sum of L1 and L2 norms of the seismograms in different wavelet channels:

$$e_l = \sum_{j=j_{\min}}^{j=jc} w_j \cdot \left(\frac{1}{k_j}\sum_{k}^{k_j}\left|o_{j,k}-y_{j,k}\right| + \sqrt{\frac{1}{k_j}\sum\left(o_{j,k}-y_{j,k}\right)^2} \right), \quad (2)$$

where $o_{j,k}$ and $y_{j,k}$ are the wavelet coefficients of the observed and synthetic seismogram for station k and wavelet index j, w_j are the weight of each wavelet channel [18].

The Green's functions used to compute the static ground displacement are calculated using the method developed by Xie and Yao[19]. We compare the observed and predicted displacements based on the mean weighted sum of the squares of the residuals

(equivalent to a reduced chi-square criterion, except that this quantity doesn't account for the number of parameters entering the model) defined as:

$$\chi_r^2 = \frac{1}{n}\sum_{i=1}^{i=n}\left(\frac{(pred^i - ob^i)}{\sigma_i}\right)^2, \quad (3)$$

where n is the number of geodetic data, σ_i is the uncertainty associated for the each measurement ob^i, $pred^i$ is the predicted displacement at site i. Because uncertainties on the InSAR data cannot be reliably estimated a priori, and because the uncertainties assigned to the GPS and coral data may not have comparable statistical meaning, we estimated a posteriori normalized uncertainties such that each data set has a reduced chi-square of 1. The normalized uncertainties assigned to each type of data were computed from the standard deviation of the misfits between the considered subset of data and the predictions of the best-fitting model derived from the joint inversion. This is achieved through an iterative scheme so that the reduced chi-square (3) calculated from the best fitting final model equals approximately 1 when only one single type of data is taken into account. The normalized uncertainties are listed in Table S6.

We have also calculated the χ_r^2 (which can also be called the mean of Weighted Residual Sum of Squares mWRSS) between the observed GPS and coral measurement and the predictions of the various models (Table S7). It shows that the residuals between the predicted and observed GPS displacements are much larger than the formal uncertainties assigned to the GPS measurements. If uncertainties were not normalized, the inversion results would be constrained almost only by the GPS data.

In addition to geodetic and seismic misfit, we constrain the solution by requiring minimization of slip difference between adjacent faults [smoothing] and minimizing the moment difference from an *a priori* value [moment constraint]. The objective function is

$$misfit = e_{WF} + W_{ST}e_{ST} + Wsm \cdot e_{SM} + W_{MO} \cdot e_{MO}, \quad (4)$$

where e_{WF} is the waveform error, W_{ST} is the weight of the static data, e_{ST} is static data error, w_{SM} and e_{SM} are weight and error for smoothness, respectively and w_{MO} and e_{SM} are weight and error for moment constraint, respectively.

All inversions start with a random initial model. The weight of the static error is then chosen to be equal to the waveform error. Weights of the constraining parameters are determined by trial and error. As the bound parameter space is searched, the objective function is minimized with 800 iterations.

References

1. Scoffin, T. P. & McLean, R. F. Exposed limestones of the northern province of the Great Barrier Reef. Philosophical Tranactions Royal Society of London, Series A 291, 119-138 (1978).

2. Taylor, F. W., Frohlich, C., Lecolle, J. & Strecker, M. Analysis of Partially Emerged Corals and Reef Terraces in the Central Vanuatu Arc - Comparison of Contemporary Coseismic and Nonseismic with Quaternary Vertical Movements. Journal of Geophysical Research-Solid Earth and Planets 92, 4905-4933 (1987).
3. Zachariasen, J., Sieh, K., Taylor, F. & Hantoro, W. S. Modern vertical deformation at the Sumatran subduction zone: Paleogeodetic Insights from Coral Microatolls. Bull.Seism.Soc.Am. 90, 897-913 (2000).
4. Briggs, R. W. et al. Deformation and slip along the Sunda Megathrust in the great 2005 Nias-Simeulue earthquake. Science 311, 1897-1901 (2006).
5. Meltzner, A. J. et al. Uplift and Subsidence Associated with the Great Aceh-Andaman Earthquake of 2004. Journal Of Geophysical Research 111, doi: 10.1029/2005JB003891 (2006).
6. Rosen, P. A., Henley, S., Peltzer, G. & M., S. Updated Repeat Orbit Interferometry Package Released,. Eos Trans. AGU 85, 47 (2004).
7. Farr, T. G. et al. The Shuttle Radar Topography Mission. Rev. Geophys. 45, RG2004 (2007).
8. Shimada, M., Isoguchi, O., Tadono, T., Higuchi, R. & Isono, K. in IGARSS07 (Barcelona, 2007).
9. Sandwell, D., Mellors, R., Shimada, M., Brooks, B. & Foster, J. Accuracy and Resolution of ALOS Interferometry: Vector Deformation Maps of the Father's Day Intrusion at Kilauea, . IEEE Geoscience and Remote Sensing Letters (2007).
10. Chen, C. W. & Zebker, H. A. Phase unwrapping for large SAR interferograms: statistical segmentation and generalized network models: . IEEE Transactions on Geoscience and Remote Sensing 40, 1709-1719 (2002).
11. Lohman, R. B. & Simons, M. Some thoughts on the use of InSAR data to constrain models of surface deformation: Noise structure and data downsampling. Geochem. Geophys. Geosyst 6 (2005).
12. Hsu, Y. J. et al. Frictional afterslip following the 2005 Nias-Simeulue earthquake, Sumatra. Science 312, 1921-1926 (2006).
13. Engdhal, E., van der Hilst, R. & Buland, R. Global teleseismic earthquake relocation with improved travel times and procedures for depth determination. Bulletin of the Seismological Society of America 88, 722-743 (1998).
14. Kieckhefer, R. M., Sho, G. G. & Curray, J. R. Seismic refraction studies of the Sunda trench and forearc basin. Journal of Geophysical Research 85, 863-889 (1980).
15. Simoes, M., Avouac, J. P., Cattin, R. & Henry, P. The Sumatra subduction zone: A case for a locked fault zone extending into the mantle. Journal of Geophysical Research-Solid Earth 109 (2004).
16. Ji, C., Wald, D. & Helmberger, D. V. Source Description of the 1999 Hector Mine, California Earthquake, Part I: Wavelet Domain Inversion Theory and Resolution Analysis. Bull. Seismol. Soc. Am. 92, 1192-1207 (2002).
17. Cotton, F. & Campillo, M. Stability of the Rake During the 1992, Landers Earthquake - an Indication for a Small Stress Release. Geophysical Research Letters 22, 1921-1924 (1995).

18. Ji, C., Wald, D. J. & Helmberger, D. V. Source description of the 1999 Hector Mine, California, earthquake, part I: Wavelet domain inversion theory and resolution analysis. Bull. Seism. Soc. Amer. 92, 1192-1207 (2002).
19. Xie, X. & Yao, Z. X. A generalized reflection-transmission coefficient matrix method to calculate static desplacement field of a dislocation source in a stratified half space. Chinese Journal of Geophysics 32, 191-205 (1989).
20. Shimada, M., Isoguchi, O., Tadono, T., Higuchi, R. & Isono, K. in IGARSS07 (Barcelona, Spain, 2007).

Figure S1 | Cumulative model fits to the InSAR data. InSAR data, and fits from the cumulative model of Fig 2a are shown. For each colored circle, the perimeter represents data point and the interior represents the model. The more similar the perimeter and interior colors, the better the fit of the model to the data.

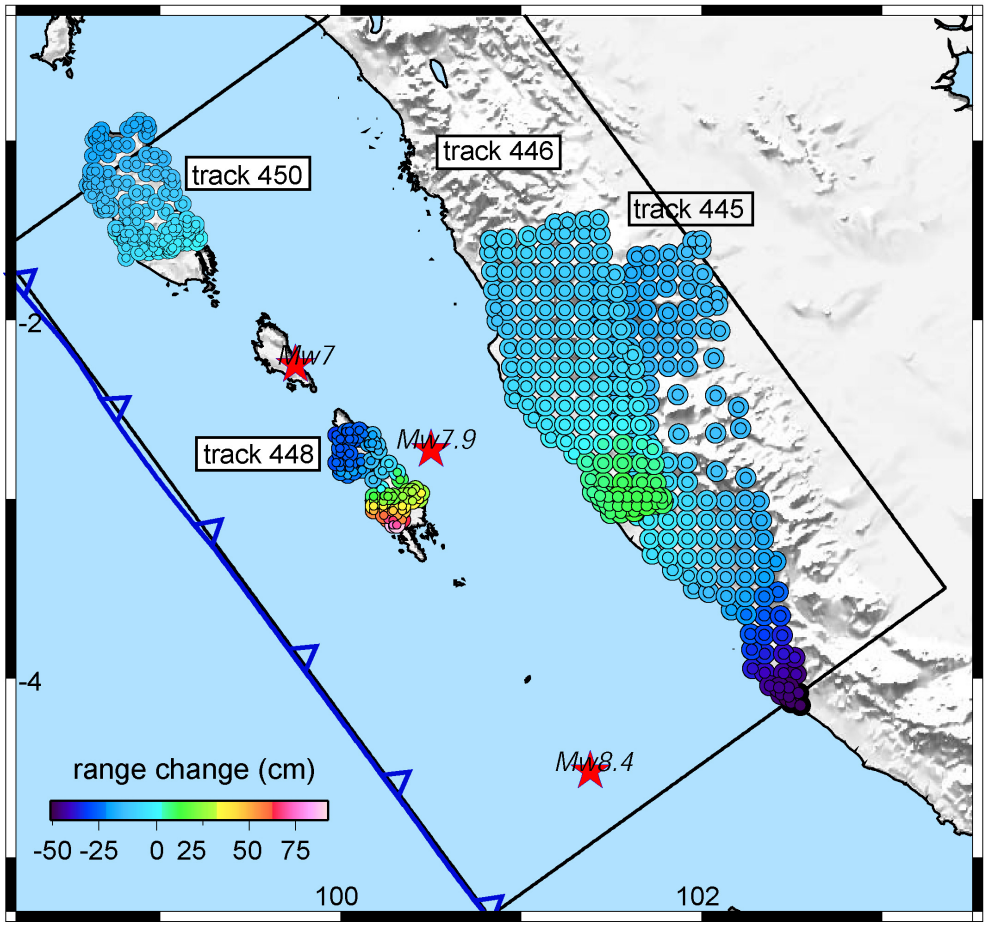

Figure S2 | Source model of the cumulative slip using coseismic measurements | a Cumulative-slip model derived from the inversion of the cGPS data only. Observed (black) and modeled (green for horizontal and gray for vertical) displacement vectors at the SuGAr GPS stations. **b** Cumulative slip obtained from addition of coseismic models of M_w 8.4 and M_w 7.9 earthquakes along with an M_w 7 aftershock located at the northwestern tip of Sipora Island. All three earthquake epicenters are shown with red stars.

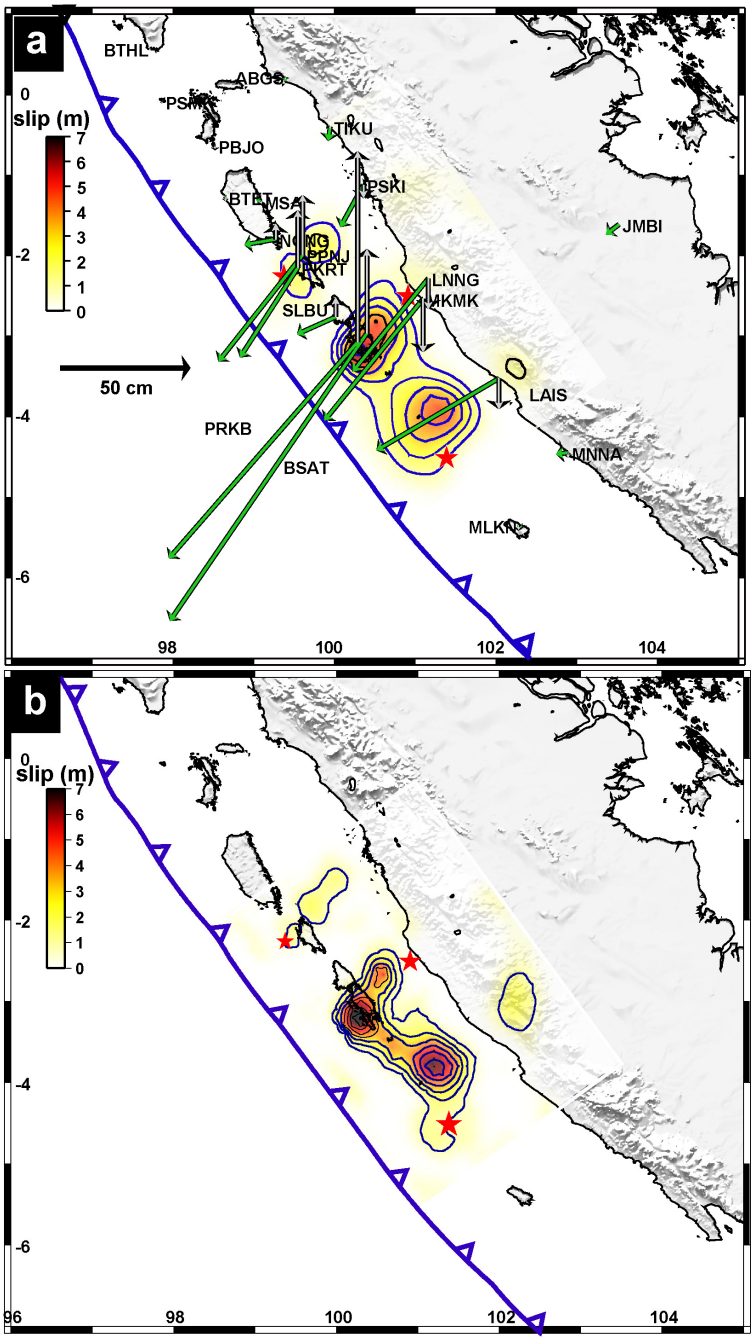

Figure S3 | Cumulative slip due to the whole earthquake sequence obtained from the inversion of the GPS and InSAR data in assuming a down-dip increase of the megathrust dip angle. Dip angle is 10° in the shallower depths (red box) and is 20° further away from the trench (orange box).

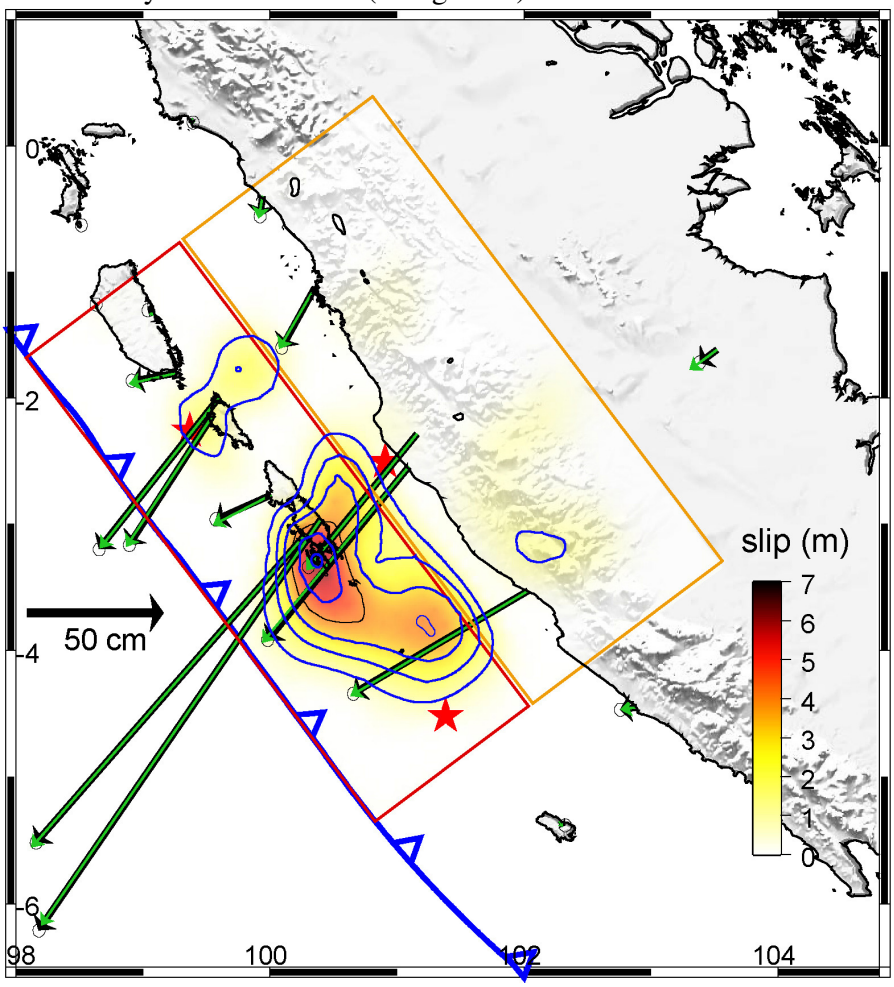

Figure S4 | Checkerboard resolution tests. a Input slip distribution corresponding to 80 km × 80 km slip patches (left) and model (right) derived from the inversion of the synthetic GPS and InSAR data. **b** Input slip distribution corresponding to 48 km × 48 km slip patches (left) and model (right) derived from the inversion of the synthetic GPS and InSAR data.

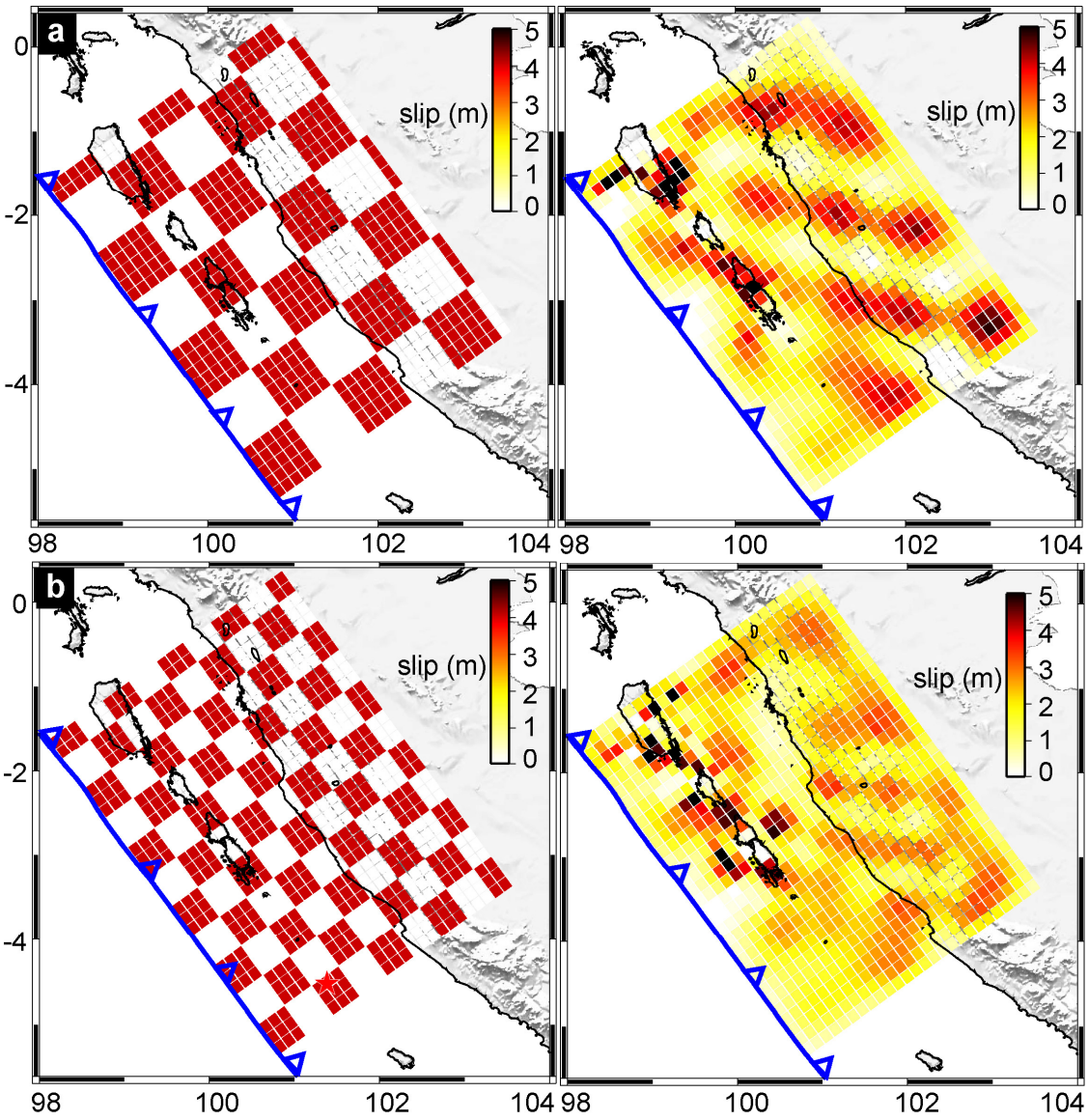

Figure S5 | Source models of M_w 8.4 and 7.9 earthquakes derived from the inversion of the teleseismic records only. Slip distribution of the M_w 8.4 earthquake **(a)**, and M_w 7.9 earthquake **(b)**.

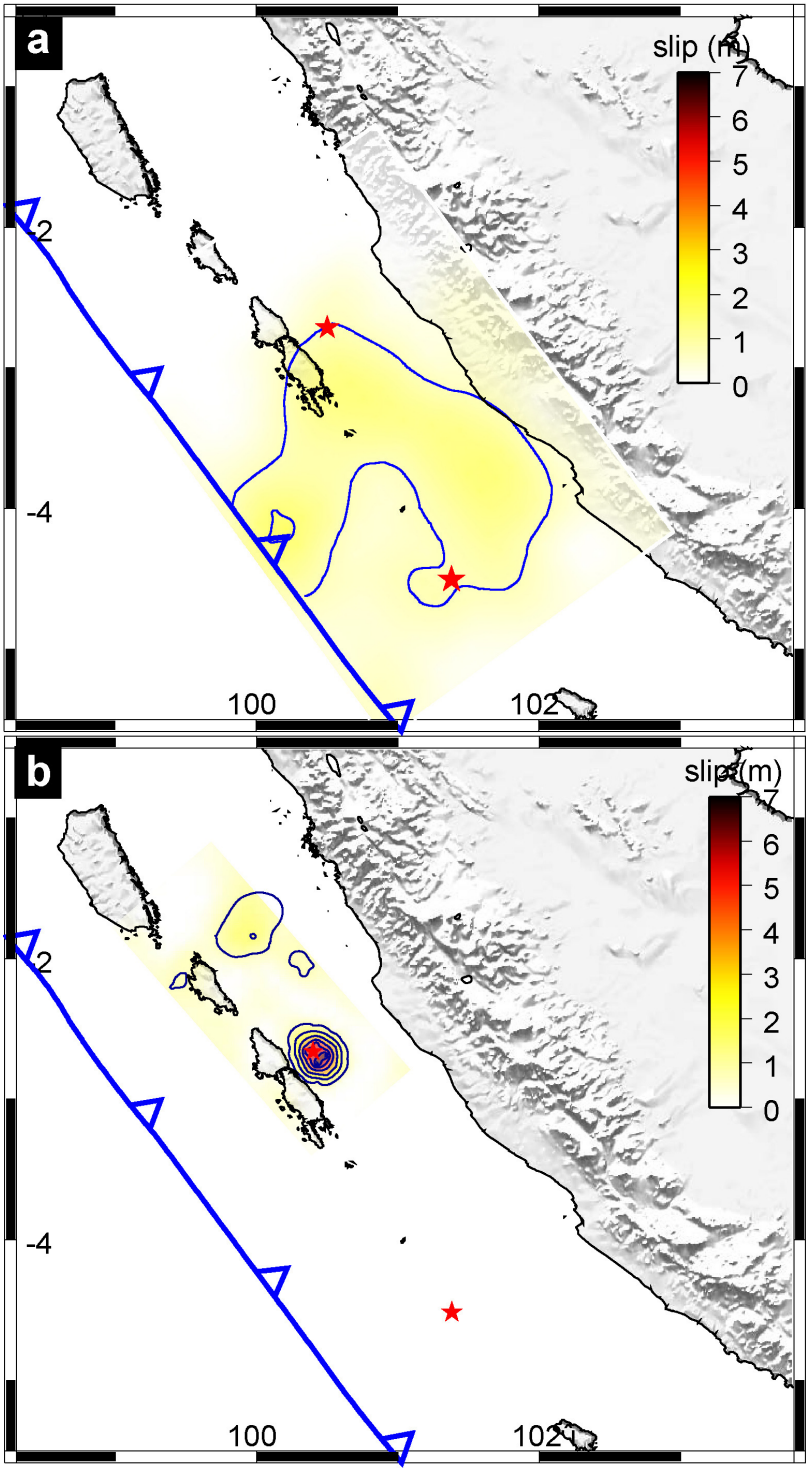

Figure S6 | Comparison of observed and predicted InSAR and teleseismic data, in the joint inversion for the M_w8.4 mainshock. a Observed and modeled LOS displacements to the InSAR data. Only the southernmost track (track 445), where the effect of the 7.9 earthquake can be assumed negligible, was used to constrain this event. For each colored circle, the perimeter represents data and the interior represents the model. The more similar the perimeter and interior colors, the better the fit of the model to the data. **b** Observed (black) and synthetic (red) teleseismic *P* and *SH* waveforms. Station name, azimuth, and distance are indicated on the left of each trace. The maximum displacement is shown at the top right of each trace in microns.

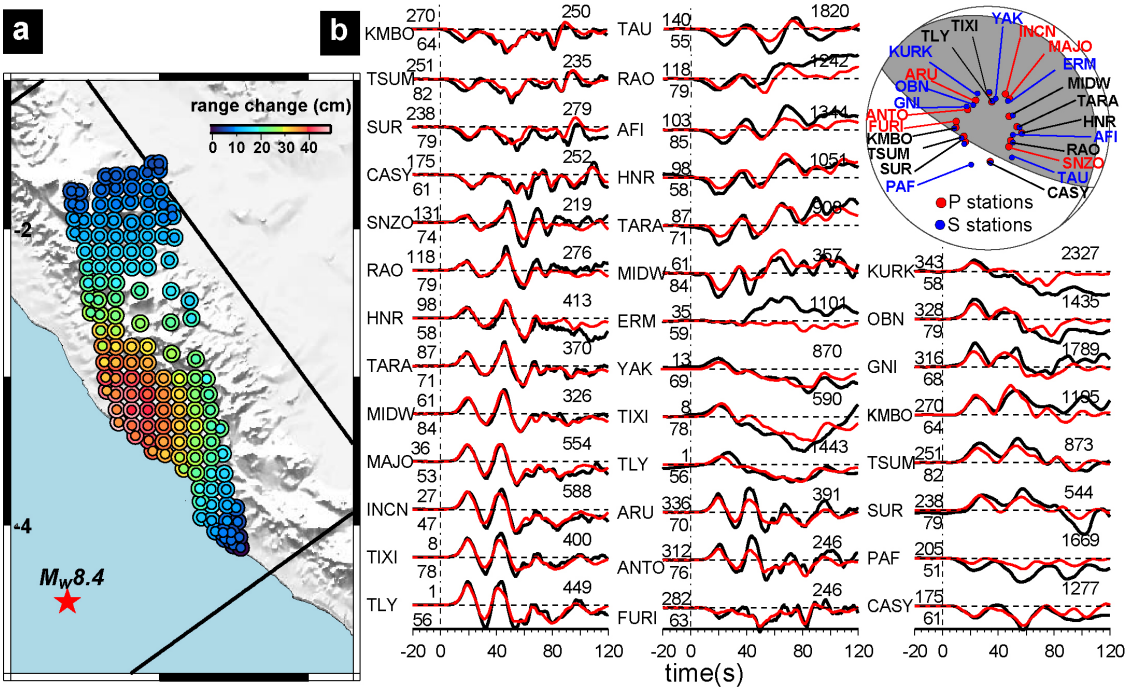

Figure S7 | M_w7.9 joint inversion model fits to the teleseismic data. Observed (black) and synthetic (red) teleseismic *P* and *SH* waveforms. Station name, azimuth, and distance are indicated on the left of each trace. The maximum displacement is shown at the top right of each trace in microns.

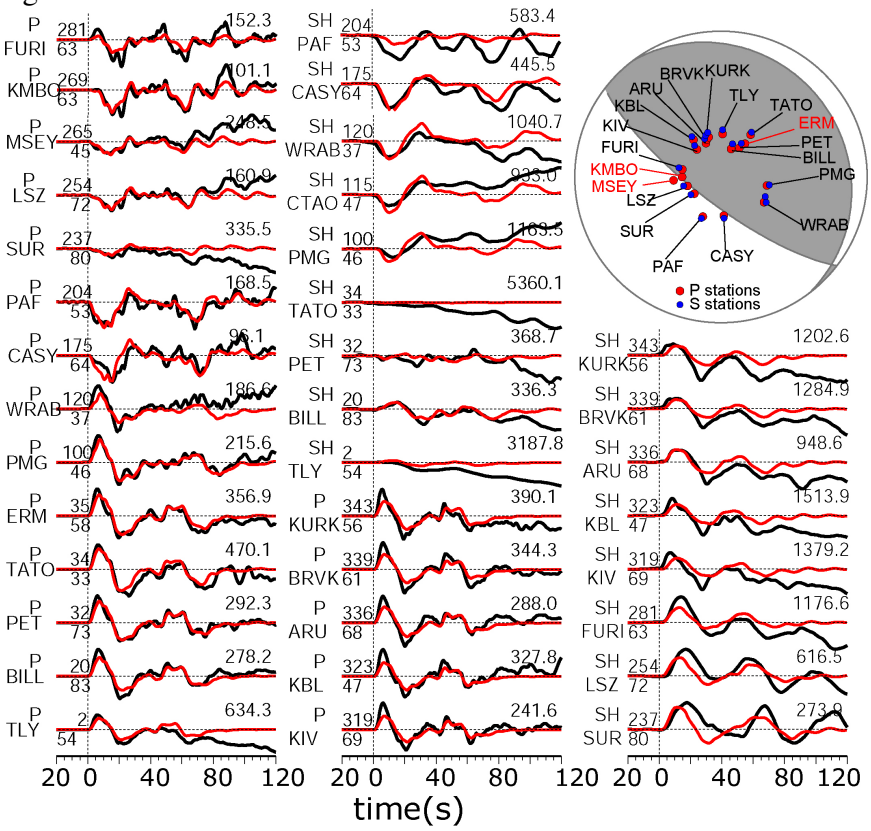

Figure S8 | Distribution of slip, isochrons and rise time for the M_w8.4 (a) and 7.9 (b) earthquakes. Top plots show the final slip distribution on the fault plane and position of the rupture front every 20 s. Arrows at each sub-fault represent the slip direction of the hanging wall relative to the footwall. Their size is proportional to slip. Rise time is defined as the duration of slip on each sub-fault.

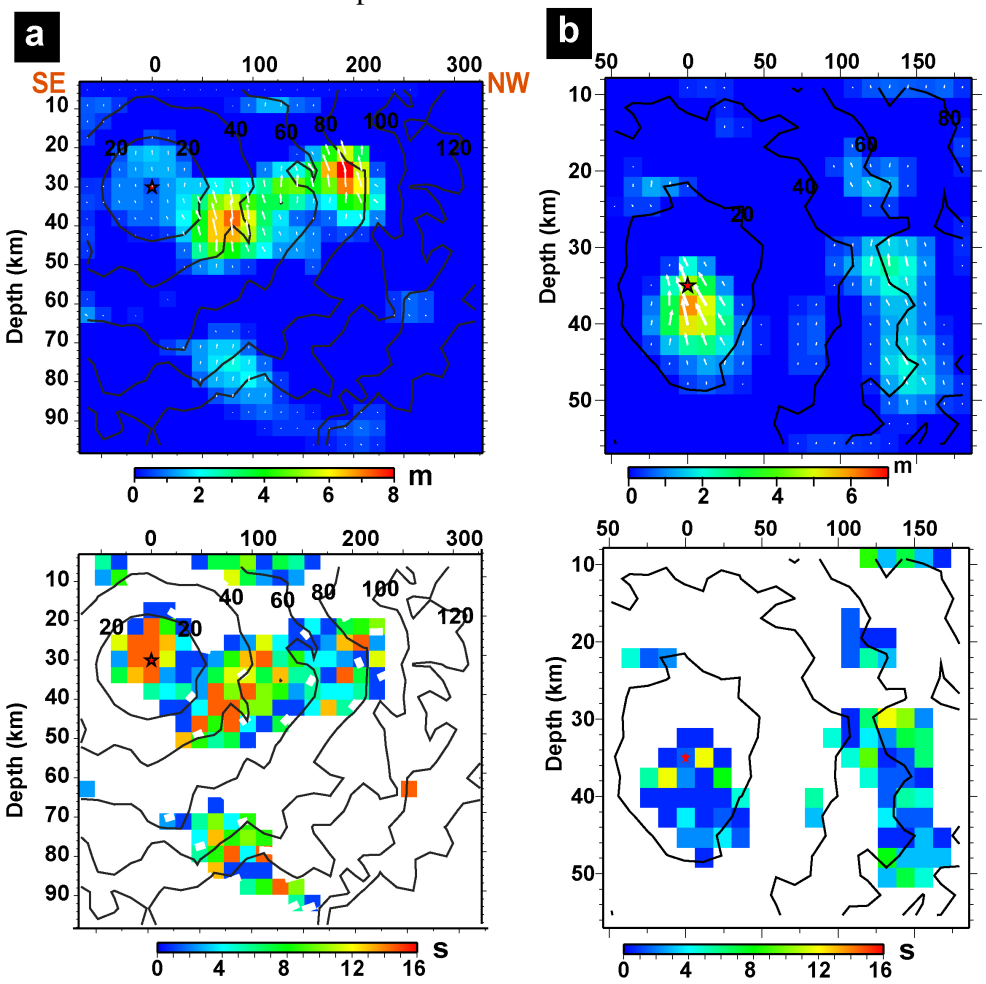

Figure S9 | Influence of a deep patch on surface displacements at LAIS. Measured horizontal (black) and vertical (blue) displacements at LAIS station are compared to model predictions when the deep slip patch is either included (model 1) or removed (model 2). "Model 1" is the model with slip down to 90 km as shown in Fig. 2b and Fig. S4a. "Model 2" has no slip deeper than 60 km, hence slip is confined to the area southwest (trenchward) of LAIS. Model 2 underestimates horizontal displacement but overestimates subsidence at LAIS. Improving the fits to the horizontal displacements worsens the fits to the vertical data, since additional slip up-dip of the LAIS station creates even greater subsidence.

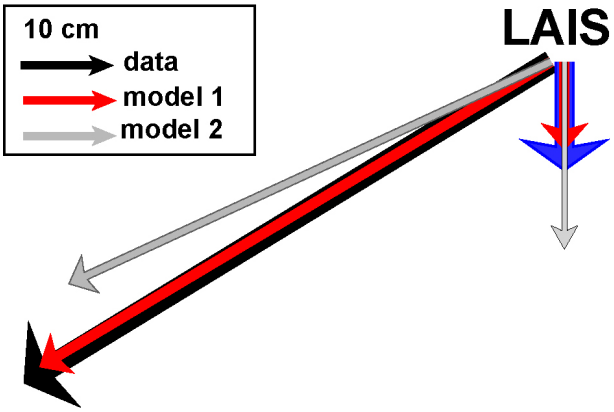

Figure S10 | Moment rate for the M_w 8.4 and M_w 7.9 events. The black and green curves show the source time functions of the mainshock and aftershock, respectively. The red curve is the source time function of the mainshock where slip patches deeper than 65 km are removed from the model. The similarity of the red and black curves shows that the deeper portion's contribution to the moment rate is very smooth, and details of the moment release are determined by the shallower slip patches.

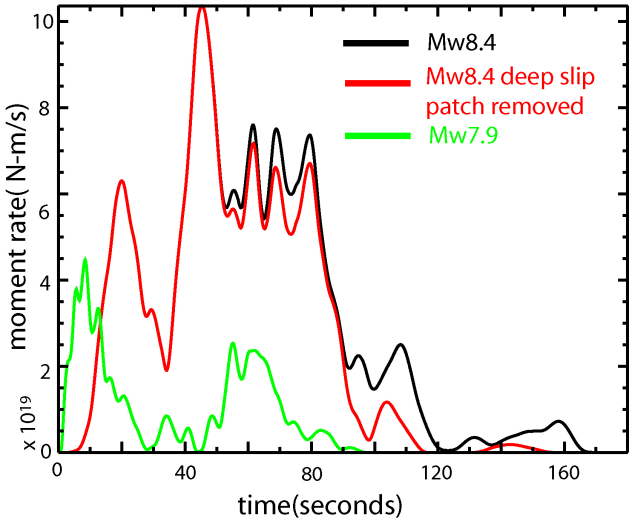

Table S1 : Cumulative co-seismic displacements due to the M_w 8.4 and 7.9 earthquakes and uncertainties derived from the GPS time series.

name	lon	lat	z	n	E	σ_z	σ_n	σ_e
ABGS	99.38749	0.22082	-0.6513	-1.6205	0.3712	0.51	0.13	0.19
BAKO	106.85000	-6.49000	-0.9400	0.5197	-0.0900	0.45	0.10	0.14
BITI	97.81137	1.07862	-0.9501	0.3598	-0.0797	0.77	0.16	0.21
BSAT	100.28456	-3.07669	72.9650	-113.0958	-98.7871	0.70	0.15	0.22
BSIM	96.32616	2.40925	-0.1753	0.5168	0.1224	0.68	0.16	0.21
BTET	98.64394	-1.28155	-1.3305	1.1137	-0.5895	0.52	0.13	0.19
BTHL	97.71070	0.56920	-0.4527	0.3365	0.0305	0.54	0.14	0.19
JMBI	103.52033	-1.61564	-0.2283	-4.7593	-6.4266	0.64	0.15	0.20
LAIS	102.03394	-3.52923	-11.7705	-37.5981	-64.0160	0.65	0.15	0.20
LEWK	95.80406	2.92359	-0.8573	0.4220	0.0490	0.52	0.14	0.18
LNNG	101.15646	-2.28531	-11.6927	-48.6283	-39.6428	0.52	0.14	0.19
MKMK	101.09140	-2.54264	-20.3530	-63.5146	-51.5661	0.53	0.14	0.19
MLKN	102.27649	-5.35255	-2.0100	-1.3571	2.2129	0.77	0.15	0.21
MNNA	102.89026	-4.45033	-1.9415	-0.8341	-6.0903	0.63	0.15	0.21
MSAI	99.08948	-1.32642	-1.2953	1.0095	-2.3344	0.69	0.16	0.22
NGNG	99.26829	-1.79959	5.7611	-2.9307	-16.4728	0.71	0.15	0.21
NTUS	103.67990	1.34580	-0.9974	-1.9993	-1.2960	0.44	0.12	0.16
PBJO	98.51571	-0.63651	-1.6725	0.3336	-0.0090	0.80	0.15	0.22
PBLI	97.40528	2.30852	0.0091	0.2268	0.1089	0.52	0.14	0.19
PKRT	99.54279	-2.15138	22.0024	-46.8171	-30.1824	0.84	0.17	0.24
PPNJ	99.60369	-1.99400	22.8536	-55.6964	-44.0273	0.60	0.14	0.20
PRKB	100.39961	-2.96660	32.1723	-150.3399	-103.1441	0.61	0.14	0.20
PSKI	100.35340	-1.12468	-4.9449	-21.9466	-12.0874	0.83	0.18	0.26
PSMK	97.86091	-0.08931	-0.6677	0.0930	-0.0754	0.60	0.14	0.19
SAMP	98.71471	3.62161	-0.7795	0.0009	-0.0001	0.61	0.15	0.20
SLBU	100.00967	-2.76634	7.4130	-9.0250	-20.2186	0.67	0.15	0.21
TIKU	99.94418	-0.39913	-0.7476	-7.3503	-1.0042	0.62	0.15	0.21

Table S2 : Co-seismic displacements due to the M_w 8.4 earthquake and uncertainties derived from the GPS time series.

name	lon	lat	z	n	e	σ_z	σ_n	σ_e
ABGS	99.38749	0.22082	-2.2354	-0.7124	1.8591	0.58	0.15	0.21
BAKO	106.85000	-6.49000	-0.0024	-0.6192	1.5462	0.52	0.12	0.15
BITI	97.81137	1.07862	-2.4067	-0.5641	1.6590	0.92	0.18	0.24
BSAT	100.28456	-3.07669	61.1763	-87.2345	-81.1502	0.83	0.18	0.25
BSIM	96.32616	2.40925	-1.6402	-0.3919	1.8470	0.80	0.18	0.23
BTET	98.64394	-1.28155	-1.3127	-0.6443	1.7655	0.61	0.15	0.21
BTHL	97.71070	0.56920	-2.7656	-0.5087	1.8299	0.60	0.15	0.21
JMBI	103.52033	-1.61564	-0.8869	-4.9008	-2.7951	0.70	0.16	0.22
LAIS	102.03394	-3.52923	-12.3301	-36.4582	-59.9395	0.74	0.16	0.23
LEWK	95.80406	2.92359	-1.9170	-0.5406	1.7558	0.58	0.15	0.20
LNNG	101.15646	-2.28531	-4.2030	-33.6649	-14.8307	0.57	0.15	0.21
MKMK	101.09140	-2.54264	-11.8656	-52.4408	-28.9090	0.64	0.15	0.21
MLKN	102.27649	-5.35255	-2.9891	-2.1924	3.4817	0.95	0.17	0.24
MNNA	102.89026	-4.45033	-2.7864	-1.4762	-4.0612	0.74	0.17	0.23
MSAI	99.08948	-1.32642	-0.5374	-0.9746	2.1352	0.71	0.16	0.22
NGNG	99.26829	-1.79959	-3.4996	-1.0757	2.1772	0.83	0.17	0.23
NTUS	103.67990	1.34580	0.2959	-1.4613	1.4697	0.48	0.13	0.17
PBJO	98.51571	-0.63651	-0.5590	-0.1682	1.9071	0.95	0.18	0.25
PBLI	97.40528	2.30852	-1.4433	-0.2905	1.8579	0.59	0.15	0.21
PKRT	99.54279	-2.15138	-3.7057	-1.2220	1.7142	1.03	0.20	0.27
PPNJ	99.60369	-1.99400	-2.6877	-1.7239	2.0305	0.67	0.16	0.22
PRKB	100.39961	-2.96660	-11.2013	-95.5292	-71.5242	0.71	0.16	0.22
PSKI	100.35340	-1.12468	-1.2549	-5.0834	1.5760	0.88	0.19	0.27
PSMK	97.86091	-0.08931	-1.8826	-0.3429	1.7369	0.69	0.16	0.22
SAMP	98.71471	3.62161	-0.3348	-0.0010	-0.0014	0.74	0.19	0.25
SLBU	100.00967	-2.76634	-1.1477	-3.1006	-3.9084	0.74	0.16	0.23
TIKU	99.94418	-0.39913	-3.8457	-3.2957	1.9442	0.73	0.17	0.24

Table S3 : Co-seismic displacements due to the M_w 7.9 earthquake and uncertainties derived from the GPS time series.

name	lon	lat	z	n	e	σ_z	σ_n	σ_e
ABGS	99.38749	0.22082	-0.5913	-0.2557	-0.8977	2.11	0.40	0.52
BAKO	106.85000	-6.49000	-0.8924	0.6740	-1.0531	1.12	0.22	0.30
BITI	97.81137	1.07862	1.6272	0.7937	-1.4707	2.46	0.39	0.51
BSAT	100.28456	-3.07669	12.9069	-22.2555	-14.0978	2.23	0.41	0.59
BSIM	96.32616	2.40925	0.6418	0.8179	-1.6020	2.11	0.40	0.51
BTET	98.64394	-1.28155	-0.5056	1.5041	-1.7813	1.79	0.35	0.47
BTHL	97.71070	0.56920	1.6883	2.7985	-1.8515	2.45	0.42	0.56
JMBI	103.52033	-1.61564	-0.0795	0.2519	-2.4870	1.85	0.36	0.50
LAIS	102.03394	-3.52923	-0.7157	0.0463	-2.0763	1.93	0.38	0.51
LEWK	95.80406	2.92359	0.5571	0.6526	-1.6152	1.63	0.34	0.45
LNNG	101.15646	-2.28531	-8.5442	-11.9588	-22.4762	1.85	0.37	0.50
MKMK	101.09140	-2.54264	-7.1612	-8.3046	-19.7675	1.57	0.33	0.46
MLKN	102.27649	-5.35255	2.0745	0.8419	-1.3896	2.57	0.39	0.53
MNNA	102.89026	-4.45033	-0.1754	0.5802	-1.1920	1.70	0.35	0.49
MSAI	99.08948	-1.32642	-0.0545	2.0363	-3.3772	1.95	0.37	0.49
NGNG	99.26829	-1.79959	7.7647	-1.3524	-17.2423	2.28	0.39	0.52
NTUS	103.67990	1.34580	-1.0845	-0.5629	-2.2186	0.95	0.24	0.30
PBJO	98.51571	-0.63651	-2.1201	0.3516	-2.0179	3.27	0.47	0.61
PBLI	97.40528	2.30852	5.7982	-0.3303	-1.5957	1.94	0.40	0.51
PKRT	99.54279	-2.15138	20.2666	-27.8907	-19.8954	2.17	0.42	0.57
PPNJ	99.60369	-1.99400	29.6427	-37.8411	-36.6640	1.69	0.34	0.47
PRKB	100.39961	-2.96660	42.3380	-51.9952	-27.6695	2.14	0.40	0.55
PSKI	100.35340	-1.12468	-5.7231	-15.5925	-12.6022	2.49	0.43	0.61
PSMK	97.86091	-0.08931	3.3596	1.4010	-0.9709	2.34	0.41	0.53
SAMP	98.71471	3.62161	0.1076	0.0012	0.0007	1.34	0.48	0.61
SLBU	100.00967	-2.76634	9.2680	-5.2968	-14.9048	1.97	0.38	0.53
TIKU	99.94418	-0.39913	1.4097	-4.1663	-1.7832	2.93	0.48	0.69

Table S4 Uplift measured from emerged coral heads.

Site	Latitude	Longitude	Measurement Date	Uplift(cm)	Uncertainty (2 σ, cm)
MEG07-A	-4.00671	101.03388	10/06/07	135	14
MEG07-B	-4.01665	101.03865	10/06/07	125	6
STP07-A	-3.45356	100.68337	10/06/07	20	12
SDG07-A	-3.48633	100.63690	10/07/07	93	23
TBO07-A	-3.34554	100.46660	10/07/07	91	14
LMS07-A	-3.20879	100.33055	10/07/07	99	23
TNP07-A	-3.16373	100.50640	10/08/07	45	12
TNK07-A	-3.18605	100.40586	10/08/07	78	23
LBT07-A	-3.11618	100.22888	10/08/07	83	6
PJS07-A	-3.01587	100.15750	10/09/07	35	12
SPG07-A	-2.88574	100.17689	10/09/07	-3	14
BSG07-A	-2.83829	100.18412	10/09/07	-19	14
TNG07-A	-2.82080	100.28000	10/09/07	-3	18
MBL07-A	-2.51578	100.01300	10/09/07	0	14
TMS07-A	-2.01886	99.61142	10/10/07	≥ 5	12
SGS07-A	-2.04684	99.65144	10/10/07	10	6
RKT07-A	-2.11664	99.70752	10/10/07	20	14
SMY07-A	-2.60447	100.11115	09/30/07	0	18

Table 5: Information about the interferograms computed from ALOS PALSAR images. All images were acquired on ascending tracks.

Region	Track	Frame numbers	Acquisition date 1	Acquisition date 2	Mode [1]	$B_\perp$(m) [2]
Bengkulu	445	7	29-Jan-07	16-Sep-07	FBS2FBD	141
	446	2	18-Aug-07	03-Oct-07	FBD2FBD	268
Pagai	448	1	06-Aug-07	21-Sep-07	FBD2FBD	506
Siberut	450	1	09-Sep-07	25-Oct-07	FBD2FBD	58

[1] FBS: Fine Beam Single Polarization (HH, 28 MHz bandwidth); FBD: Fine Beam Dual polarization (HH and HV, 14 MHz) [20].

[2] $B_\perp$ is the perpendicular baseline, that is, the component of the orbital separation perpendicular to the line of sight.

Table S6: Misfits and normalized uncertainties.

Model	Moment (N-m)	Waveform Misfit	GPS (cm)			Coral (cm)	InSAR (cm)
			σ_e	σ_n	σ_z		
Cumulative (GPS only)	7.3×10^{21}	-	0.9	1.	0.9	-	-
Cumulative (all data)	7.5×10^{21}	-	0.9	1.1	1.0	11.15	1.48
M_w 8.4	5.15×10^{21}	0.14	2.4	2.2	4.1	7.4	3.6
M_w 7.9	1.13×10^{21}	0.25	2.6	2.6	2.3	-	-
M_w 7.0	4.7×10^{19}	-	1.7	2.2	1.5	-	-

Table S7: Weighted Root Mean Square (WRSS) of residuals between the predicted and observed GPS and coral measurements.

Model	GPS			Coral
	E	N	Z	
Cumulative (all data)	18.4	36	6.2	5
M_w8.4	59.2	72	5.4	1.6
M_w7.9	8	7.4	1.5	-